

Exploring entanglement in open cavity parametric oscillators: from triply to doubly resonant cavities

Bárbara Abigail Ferreira Ribeiro,^{1,*} Rayssa Bruzaca de Andrade,^{1,†} Marcelo Martinelli,¹ and Breno Marques^{1,2,‡}

¹*Instituto de Física, Universidade de São Paulo, P O Box 66318, 05315-970 São Paulo, Brazil*

²*Ciências Naturais e Humanas, Universidade Federal do ABC - UFABC, Santo André, Brazil*

We use a versatile model to evaluate the multipartite entanglement and the nonclassical light generation in optical parametric oscillators, exploring the differences between doubly and triply resonant cavity configurations. We demonstrate the entanglement of the pump mode with converted fields in both situations, and the fundamental differences of oscillators using parametric down conversion and four wave mixing processes as the intracavity amplification technique. The strong correlations involving the sidebands of the pump and converted fields gives the signatures of a rich dynamic of multipartite entanglement.

I. INTRODUCTION

Initially presented as a frequency converter that produces tunable coherent radiation [1], the simplest configuration of an Optical Parametric Oscillator (OPO) was showed to be a source of multiple non-classical states of light. The long list includes squeezed states [2, 3], quantum correlated beams [4, 5], entangled thermal states [6], and multicolor entanglement for two [7, 8], three [9], and up to six modes of the field [10]. This versatile source has found applications in quantum metrology [11] and quantum communication protocols, such as quantum key distribution [12] and quantum teleportation [13]. Moreover, extensions over the basic configuration allowed the generation of cluster states with arbitrarily large number of modes [14, 15] as a possible resource for quantum computation [16].

The usual configuration consists of a non-linear medium inside an optical cavity. The nonlinear medium will couple the pump field to a pair of modes named signal and idler, often through a second ($\chi^{(2)}$) or third ($\chi^{(3)}$) order non-linearity. Energy exchange among these three fields will follow both energy and momentum conservation [17]. The nonlinear medium acts as a parametric amplifier and, if amplification matches the cavity losses, the oscillation threshold is reached and we have the generation of intense output fields. Even for this simple case we may have distinct cavity configurations [18]. The cavity may be either resonant for all three modes (triply resonant OPO - TROPO), for both converted fields (doubly resonant OPO - DROPO), or just for one of them (singly resonant OPO - SROPO).

Quantum treatment of a TROPO using a $\chi^{(2)}$ medium was extensively done in both operation regimes (below [19, 20] and above threshold [21, 22]). This treatment applies for the DROPO as well, as far as the pump depletion is negligible. That is the case far below the oscil-

lation threshold, where pump is treated just as a classical field. To the best of our knowledge, a full quantum treatment for the DROPO and the effects of pump depletion on the quantum noise is missing. Here we use the multimode analysis of the cavity evolution [23] to compare the noise and the quantum correlations of DROPO and TROPO in above threshold operation, demonstrating that multipartite entanglement and the squeezing of the pump noise are present even in a single pass regime.

The model has the advantage of being applicable to open cavities, beyond the closed cavity regime adopted in typical input/output formalism [24, 25]. That is particularly interesting for the study of $\chi^{(3)}$ OPOs, and we compare their behavior to the usual $\chi^{(2)}$ oscillator above threshold. The small gain, typically found in $\chi^{(2)}$ amplifiers based on parametric down conversion (PDC), leads to high reflectance mirrors (typically greater than 95%) for continuous operation even for the best available crystals. On the other hand, although many oscillators based on four wave mixing (4WM) will present a closed cavity [26], this process can be much stronger in atomic vapors [27], where the $\chi^{(3)}$ process is enhanced close to the atomic transitions. This enable the development of OPOs with higher transmittance mirrors (open cavity) [28, 29].

We begin by a description of the classical behavior of an OPO considering the DROPO and the TROPO case without any approximation for the reflections coefficients of the cavity (section II), accounting for the evolution of the mean fields along the gain medium (both $\chi^{(2)}$ and $\chi^{(3)}$). We go beyond the studies of the classical behavior of $\chi^{(2)}$ [30] that accounts only for the first order of the expansion to compute the mean fields, which is not appropriate to simulate a $\chi^{(3)}$ OPO with a higher gain [29]. Afterwards, we provide a quantum description of the systems considering the quantum treatment of the fluctuations in terms of the symmetric and antisymmetric basis of the electromagnetic field yielding a full description of the state of the fields in terms of a covariance matrix (section III). Next, we evaluate the quantum features generated by different types of OPO (section IV), squeezing, bipartite and multipartite entanglement, showing the main differences that appear on each

*B.A.F.R. and R.B.A. contributed equally for this project.

†Electronic address: rabda@fysik.dtu.dk

‡Electronic address: breno.marques@ufabc.edu.br

configuration.

II. CLASSICAL APPROACH

We evaluate the evolution of the mean field during the parametric amplification in both cases, PDC and 4WM, before considering the steady state conditions inside a cavity. The cavity feedback will lead to a dramatic effect of gain saturation, completely modifying the response of the free propagating process.

Using a medium with second (third) order non-linearity, one (two) photon(s) of the pump beam (of frequency ω_1) might be converted into two photons, signal and idler (with respective frequencies ω_1 and ω_2). The interaction Hamiltonians $\hat{H}^{(2)}$, which represents the PDC, and $\hat{H}^{(3)}$, representing the 4WM, are given by:

$$\hat{H}^{(2)} = i\hbar\chi^{(2)}\hat{a}_0(t)\hat{a}_1^\dagger(t)\hat{a}_2^\dagger(t) - h.c., \quad (1)$$

$$\hat{H}^{(3)} = i\hbar\chi^{(3)}\hat{a}_0^2(t)\hat{a}_1^\dagger(t)\hat{a}_2^\dagger(t) + h.c., \quad (2)$$

in the interaction picture. Here \hat{a}_n , with $n = \{0, 1, 2\}$, represents the annihilation operators of the pump, signal and idler modes, respectively, and the parameter $\chi^{(m)}$ with $m = \{2, 3\}$ is associated with the non-linear susceptibility coefficient of each gain medium.

In order to determine the mean amplitudes of the output fields as a function of the system parameters, the operators evolution $\hat{a}_n(t)$ through the gain medium are evaluated through the Heisenberg equations for the field operators, $\frac{d}{dt}\hat{a}_n(t) = (i/\hbar)[\hat{H}^{(m)}, \hat{a}_n(t)]$. Linearizing the field operators as $\hat{a}_n(t) = \alpha_n + \delta\hat{a}_n(t)$, where α_n is the mean field amplitude and $\delta\hat{a}_n(t)$ is the field fluctuations, the set of expressions that describe the mean value evolution of the fields α_n through the gain medium can be written as:

$$\frac{d\alpha_0}{dt} = -(m-1)\chi^{(m)}\alpha_0^{*(m-2)}\alpha_1\alpha_2, \quad (3a)$$

$$\frac{d\alpha_1}{dt} = \chi^{(m)}\alpha_0^{(m-1)}\alpha_2^*, \quad (3b)$$

$$\frac{d\alpha_2}{dt} = \chi^{(m)}\alpha_0^{(m-1)}\alpha_1^*, \quad (3c)$$

where α_n^* is the complex conjugate of α_n . The mean value of the field is a complex number that can be explicitly written in terms of real amplitude and phase: $\alpha_n = \sqrt{P_n}e^{i\theta_n}$. The parameter $P_n = \alpha_n\alpha_n^*$ is proportional to the photon number in the field n and hence to the field power. Differentiating P_n in time we have

$$\frac{d}{dt}P_n = \alpha_n\frac{d\alpha_n^*}{dt} + \alpha_n^*\frac{d\alpha_n}{dt}, \quad (4)$$

and with the help of Eq.(3), we have a set of differential

equations that describe the evolution of P_n

$$\begin{aligned} \frac{dP_0}{dt} &= -2(m-1)\chi^{(m)}\sqrt{P_0^{(m-1)}}P_1P_2\cos\theta, \\ \frac{dP_1}{dt} &= 2\chi^{(m)}\sqrt{P_0^{(m-1)}}P_1P_2\cos\theta, \\ \frac{dP_2}{dt} &= 2\chi^{(m)}\sqrt{P_0^{(m-1)}}P_1P_2\cos\theta, \end{aligned} \quad (5)$$

depending on a global phase $\theta = \theta_1 + \theta_2 - (m-1)\theta_0$. In practice, the exact value will depend on the phase matching condition, involving the value of $\chi^{(m)}$ and on the reflection coefficient of the mirrors [30], but the general effect will be the modulation of the coupling. Therefore, we will chose θ that maximizes the coupling, thus $\cos(\theta) = 1$. A detailed evaluation of the field evolution for the case of a $\chi^{(2)}$ medium is given in [31].

As the fields propagate along the gain medium, we may evaluate the power transfer from the pump to the converted modes. The number of photons of the pump will be reduced, leading to $P_0(t) = P_0(0) - (m-1)p(t)$. This photon depletion leads to a change in the photon number of the converted fields as $P_1(t) = P_1(0) + p(t)$ and $P_2(t) = P_2(0) + p(t)$. Considering a balanced power for converted modes, $P_1(t) = P_2(t)$, therefore the set of Eqs. (5) can be used to obtain the evolution of $p(t)$, related with the power transfer along the path. For convenience,

$$\frac{dp}{dt} = 2\chi^{(m)}(P_0(0) - (m-1)p)^{\frac{1}{2}(m-1)}(P_1(0) + p). \quad (6)$$

The total power variation of signal field, $\Delta P_1^{(m)}$, for each gain medium m , will be computed integrating Eq. (6) in the limits of the entrance $(t_1, p(t_1)) = (0, 0)$, and the end $(t_2, p(t_2)) = (L/(nc), \Delta P_1^{(m)})$ of the gain medium of length L , where c is the velocity of light in the vacuum and n is the refractive index. Considering the $\chi^{(2)}$ gain medium we have

$$\begin{aligned} \Delta P_1^{(2)} &= P_0(0) - (P_0(0) + P_1(0)) \\ &\quad \times \tanh^2 \left[\kappa^{(2)} \sqrt{P_0(0) + P_1(0)} \right. \\ &\quad \left. - \operatorname{arctanh} \left[\sqrt{\frac{P_0(0)}{P_0(0) + P_1(0)}} \right] \right], \end{aligned} \quad (7)$$

with $\kappa^{(m)} = \chi^{(m)}L/(nc)$. Although this equation is not simple, in the limit of a weak coupling we have $\Delta P_1^{(2)} = \kappa^{(2)}/P_1(0)\sqrt{P_0}$, recovering the situation observed in [30]. For a $\chi^{(3)}$ gain medium we obtain

$$\Delta P_1^{(3)} = \frac{P_0(0)P_1(0) \left(e^{2\kappa^{(3)}(P_0(0)+2P_1(0))} - 1 \right)}{2P_1(0)e^{2\kappa^{(3)}(P_0(0)+2P_1(0))} + P_0(0)}. \quad (8)$$

In the $\chi^{(3)}$ scenario, it is interesting to evaluate the signal (and idler) relative gain $G^{(3)}$. From Eq. (8) we

have

$$G^{(3)} = \frac{\Delta P_1^{(3)}}{P_1(0)} = \frac{g^{(3)} - 1}{1 + 2g^{(3)}P_1(0)/P_0(0)}, \quad (9)$$

where $g^{(3)} = \exp[2\kappa^{(3)}(P_0(0) + 2P_1(0))]$ corresponds to the unsaturated amplification. For a completely open cavity and a weak seed ($P_1(0) \ll P_0(0)$), Eq. (9) simplifies as

$$G^{(3)} + 1 = e^{2\kappa^{(3)}P_0(0)} = g^{(3)}. \quad (10)$$

The amplification then increases exponentially with the pump power and the medium length, which is proportional to $\kappa^{(3)}$. This is the typical situation of unsaturated parametric amplifier as used in [27]. It also becomes evident the role of an increasing seed: it will lead to a saturation of the power transfer process, and therefore a reduction of the gain in Eq. (9).

From Eq. (7) and (8), we can relate the added power on the converted fields to the coupling coefficients $\kappa^{(m)}$, and the field power at the input of the amplifier, $P_0(0)$ and $P_1(0)$. This result is used now to evaluate the intra-cavity steady state. First, we compare the solutions for both gain media in a doubly resonant cavity in Section II A, where pump beam makes a single pass through the cavity while signal and idler beams are resonant. Next, in Section II B, we consider a triply resonant OPO, exploring different reflections of the input mirror for the pump field.

A. Doubly Resonant Optical Parametrical Oscillator

The first system being studied is a DROPO (Fig. 1). For convenience, we will label the power at the input and the output of the medium by the positions 0 and L . In this case, the pump beam makes a single pass through the cavity, therefore the pump power injected in the cavity defines $P_{0in} = P_0(0)$. When it leaves the cavity, the output power is given by $P_{0out} = P_0(L) = P_{0in} - (m-1)\Delta P_1^{(m)}$.

In the steady state, we can relate the input power of the signal to the output of the amplifier using the reflectance R_1 on the output coupler M_{PT} , as $P_1(0) = R_1P_1(L)$. The output of the OPO will be related to the output of the amplifier as well $P_{1out} = (1 - R_1)P_1(L)$. From the definition of $\Delta P_1^{(m)} = P_1(L) - P_1(0)$ we can calculate the output power P_{1out} as

$$P_{1out} = \frac{(1 - R_1)P_1(0)}{R_1} = \Delta P_1^{(m)}. \quad (11)$$

This result is already expected from a cavity in equilibrium due to energy conservation: the energy added to a given mode will match the losses through the output

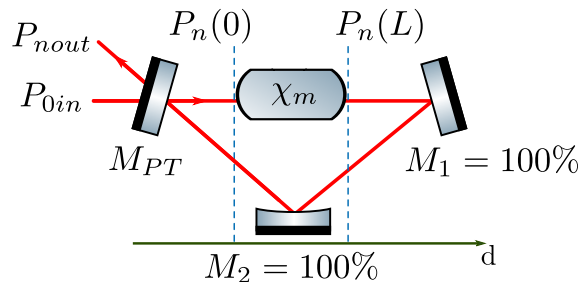


FIG. 1: OPO model using a ring cavity with two highly reflective mirrors ($M_1 = M_2 = 1$), an output coupler M_{PT} and a gain medium with length L . The M_{PT} reflectance coefficient for the pump beam is R_0 and for both, signal and idler beams, R_1 .

coupler.

Numerical solution of Eq. (11), combined with Eq. (7) (for $\chi^{(2)}$) and Eq. (8) (for $\chi^{(3)}$) gives the value of $P_1(0)$ as a function of the pump power P_{0in} . Evaluation of the output power P_{1out} is immediate. The result is presented in Fig. 2(a), for the $\chi^{(2)}$ gain medium, giving an output power close to the parabolic curve deduced in [31]. On the other hand, in Fig. 2(b), for the $\chi^{(3)}$ gain medium, we can observe that the curve approaches a proportional response for sufficiently high pump power. Even close to the threshold, as showed in the inset, the evolution could be closely approximated by a linear response when the cavity coupling is higher, as observed in [29]. The asymptotic behavior is similar for the distinct couplings, and very different from the one observed with $\chi^{(2)}$. The insets put in evidence the reduction of the threshold power for a reduction of the cavity losses. The chosen value of the nonlinearity $\kappa^{(3)} = 3W^{-1}$ is based on the observed amplification in [27]. The value of $\kappa^{(2)} = 0.5W^{-1/2}$ is chosen to match the threshold power for both media with $R_1 = 0.85$. We will adopt this value for the simulations along the remaining of the article.

Although the power has some dramatic changes for distinct coupling, a better comparison can be done using the conversion efficiency

$$\eta = \frac{\hbar\omega_1 P_{1out} + \hbar\omega_2 P_{2out}}{\hbar\omega_0 P_{0in}}. \quad (12)$$

The efficiency is showed in Fig. 3, with the pump power normalized to the threshold power. The conversion efficiency increases monotonically in both cases, but the most relevant difference between $\chi^{(2)}$ and $\chi^{(3)}$ amplifiers comes from the fact that a maximum (unitary) efficiency is observed at a pump power $\simeq 4$ times above threshold for $\chi^{(2)}$ oscillators, while $\chi^{(3)}$ oscillators evolve asymptotically to unitary gain. Notice as well that while the unitary efficiency for $\chi^{(2)}$ is reached at $\sigma_{max} \simeq 4$ for a closed cavity, the position of the maximum is reduced when cavity losses are increased, as observed in [31].

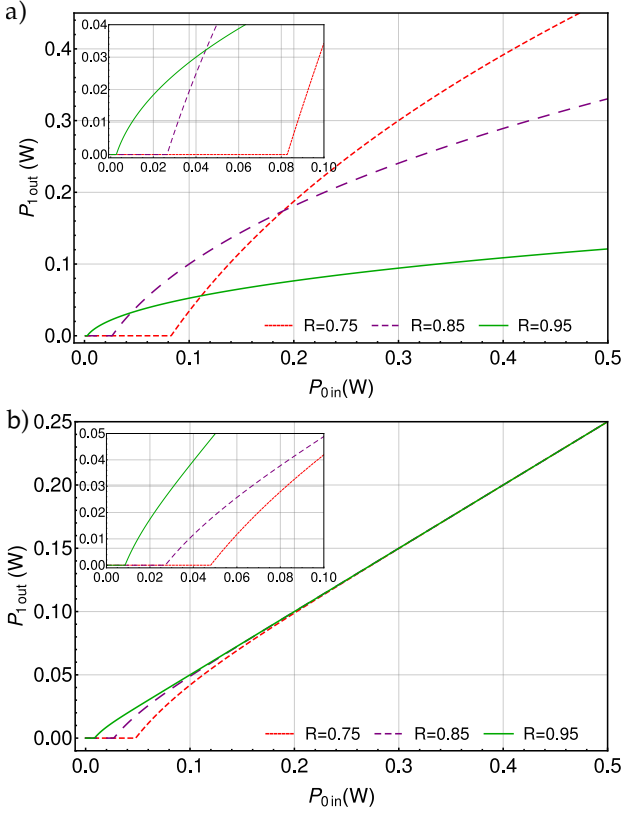


FIG. 2: DROPO: P_{out} as a function of P_{in} for different reflectivity coefficients $R_1 = \{75\%, 85\%, 95\%\}$. Simulations considering (a) a $\chi^{(2)}$ gain medium with $\kappa^{(2)} = 0.5W^{-1/2}$ and in (b) a $\chi^{(3)}$ gain medium with $\kappa^{(3)} = 3W^{-1}$.

B. Triply Resonant Optical Parametrical Oscillator

We have now a cavity for the pump that enhances its power, what makes this system being called pump enhanced DROPO as well. Self-consistency equation for the converted field, Eq. (11), is still valid. However the self consistency equations will differ for the pump field that now includes a beam splitter transformation for the input coupler:

$$\sqrt{P_0(0)} = t_0\sqrt{P_{0in}} - r_0\sqrt{P_0(L)} \quad (13)$$

$$\sqrt{P_{0out}} = t_0\sqrt{P_0(L)} + r_0\sqrt{P_{0in}}, \quad (14)$$

where $r_0 = \sqrt{R_0}$ is the reflection coefficient and $t_0 = \sqrt{1 - R_0} = \sqrt{T_0}$ is the transmission coefficient.

The output pump power in terms of the input pump power P_{0in} and the intracavity pump power $P_0(0)$ is obtained by combining Eqs. (13) and (14):

$$P_{0out} = \frac{P_{0in} - 2t_0\sqrt{P_{0in}P_0(0)} + T_0P_0(0)}{R_0}. \quad (15)$$

We would like to evaluate the behavior of P_{1out} in

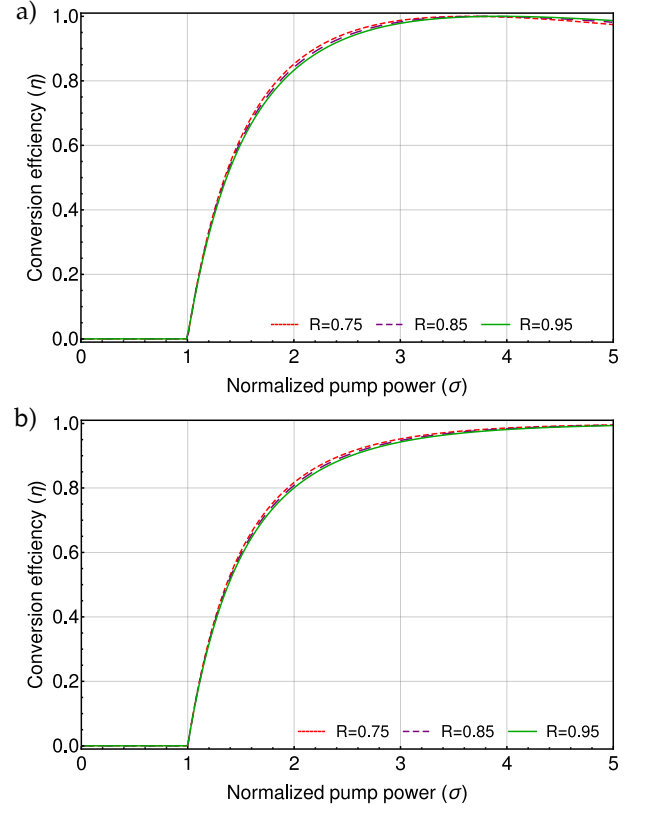


FIG. 3: DROPO: Conversion efficiency η as a function of pump power (normalized by the threshold power) σ for $R_1 = \{75\%, 85\%, 95\%\}$. Simulations with a) a $\chi^{(2)}$ gain medium and b) a $\chi^{(3)}$ gain medium.

terms of P_{0in} . A numerical solution for this quantity can be obtained by evaluating the intracavity fields $P_0(0)$ and $P_1(0)$ as a function of the input power, the coupling constant $\kappa^{(m)}$ and the mirror reflectances $R_0, R_1 = R_2$. As an example, a detailed evaluation of the output power for $\chi^{(3)}$ TROPO is performed in the Appendix A.

For the moment we will consider that the cavity mirrors have the same reflectance for pump, signal and idler beams, $R_0 = R_1 = R_2 = R$. While this situation is quite unusual for $\chi^{(2)}$ OPOs, it is common for the $\chi^{(3)}$ condition, when all the resonant fields may be nearly degenerate in frequency, leading to balanced losses. In this situation a direct equation for the intracavity fields and the pump power can be obtained.

In a steady state the total intracavity power, P_{T0} , is constant at any point inside the cavity, resulting in the relation $P_{T0} = P_0 + (m - 1)P_1$. Due to energy conservation, the relation between the input pump field and the output fields of the cavity is $P_{0in} = P_{0out} + (m - 1)P_{1out}$, where P_{1out} is given by Eq. (11). Now it is possible to rewrite the intracavity fields, $P_0(0)$ and $P_1(0)$, in terms of the input pump power P_{0in} , and the total intracavity pump power, P_{T0} . From the above description, combined

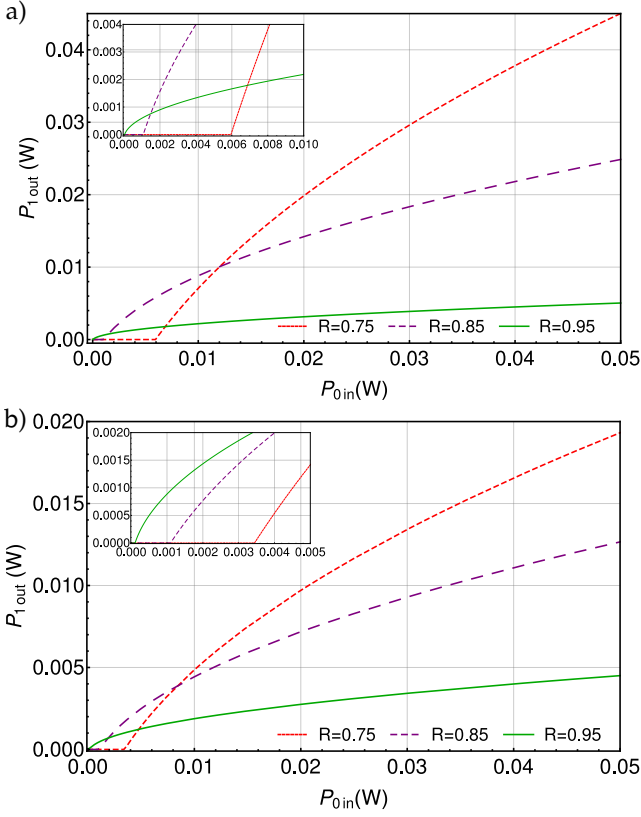


FIG. 4: TROPO: P_{1out} in function of P_{0in} for different reflectivity coefficients $R_1 = \{75\%, 85\%, 95\%\}$. Simulations considering a) a $\chi^{(2)}$ gain medium and in b) a $\chi^{(3)}$ gain medium.

with Eqs. (13) and (15), we obtain

$$P_0(0) = \frac{1 - R (P_{0in} + P_{T0})^2}{4 P_{0in}}, \quad (16)$$

$$P_1(0) = \frac{R - 1}{4(m - 1)} \frac{(P_{0in} - P_{T0})^2}{P_{0in}} + \frac{R P_{T0}}{m - 1}, \quad (17)$$

where Eq. (16) and Eq. (17) describe the behavior of $P_0(0)$ and $P_1(0)$ as a function of P_{T0} and P_{0in} .

The problem now becomes writing P_{T0} as a function of the input pump power, P_{0in} . In the $\chi^{(2)}$ TROPO configuration, by equalling Eq. (7) and Eq. (11) results in

$$\frac{(1 - R)(P_{0in} - P_{T0})^2}{4R P_{0in} P_{T0}} = \tanh^2 \left[\kappa^{(2)} \sqrt{P_{T0}} - \operatorname{arctanh} \left[\sqrt{(1 - R) \frac{(P_{0in} + P_{T0})^2}{4P_{0in} P_{T0}}} \right] \right], \quad (18)$$

which is used to find a numerical solution to P_{T0} as a function of P_{0in} . Considering the $\chi^{(3)}$ TROPO, the treatment consists of equalling Eq. (8) to Eq. (11). Rearranging the terms we obtain $\frac{P_1(0)}{P_0(0)} = \frac{R e^{2\kappa_3 P_{T0}} - 1}{2(1 - R) e^{2\kappa_3 P_{T0}}}$ and substituting Eq. (16) and Eq. (17) in the later expression

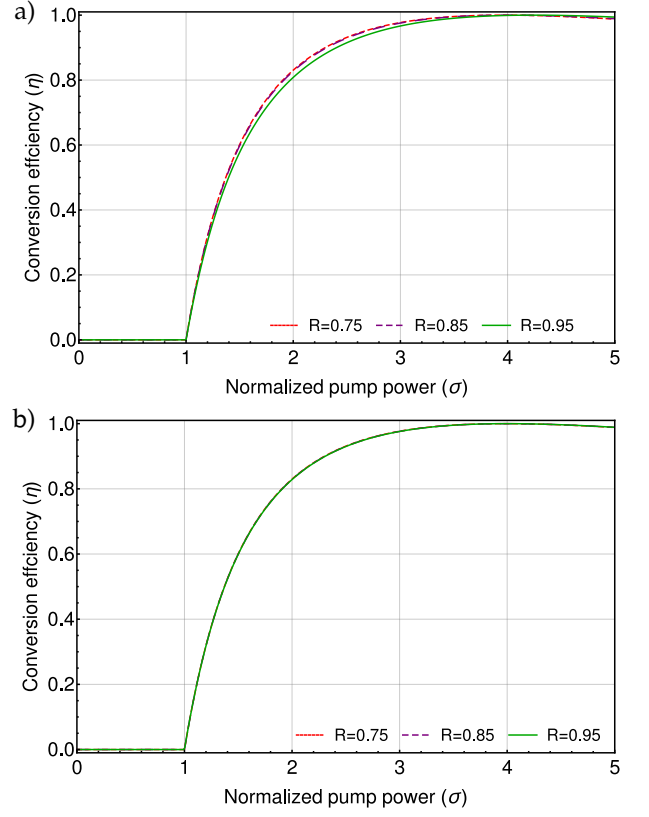


FIG. 5: TROPO: η in function of σ for $R_1 = \{75\%, 85\%, 95\%\}$. Simulations with a) a $\chi^{(2)}$ gain medium and b) a $\chi^{(3)}$ gain medium.

results in:

$$(1 - R)(P_{0in} - P_{T0})^2 - 4R P_{0in} P_{T0} = (e^{-2\kappa_3 P_{T0}} - R)(P_{0in} + P_{T0})^2, \quad (19)$$

enabling a numerical solution for P_{T0} as a function of P_{0in} . Using equations Eq. (18) and Eq. (19) as an input in equation Eq. (17) we have $P_1(0)$ as a function of P_{0in} for $\chi^{(2)}$ and $\chi^{(3)}$ TROPO, respectively. In order to evaluate the behavior of P_{1out} as a function of P_{0in} we just replace $P_1(0)$ in Eq. (11).

The behavior of P_{1out} as a function of P_{0in} is showed for a $\chi^{(2)}$ gain medium in Fig. 4 (a) and for a $\chi^{(3)}$ gain medium in Fig. 4 (b). The behavior of both systems are analysed for three different reflection coefficients and the increase in the threshold power can be observed when R changes from $R = 95\%$ to $R = 75\%$. Furthermore, the converted fields power increases with the input pump power, but differently from the DROPO, both curves present a parabolic-like shape.

A better comparison of the curves can be obtained from the conversion efficiency, as showed in Fig. 5. The maximum conversion efficiency occurs approximately in $\sigma = 4$ decreasing from this point on to approximately 50% for $\sigma \gg 4$. The behavior for the different reflectivity coefficient is very similar in all σ analysed for both

$\chi^{(2)}$ and $\chi^{(3)}$ TROPO in the presented range.

These results are similar to those obtained for $\chi^{(2)}$ OPOs, as presented in [30, 31]. The main point of the present treatment is to obtain a detailed evolution of the mean fields inside the gain medium. That is a fundamental part in the evaluation of the noise for a cavity in the open limit, beyond the first order approximation for the mean field, as we demonstrate now.

III. THEORETICAL DESCRIPTION OF THE FIELD QUANTUM FLUCTUATIONS

In order to evaluate the quantum fluctuations as a function of the oscillator parameters in the spectral domain, we follow the formalism described in [23]. We begin by writing the time-dependent annihilation operator in terms of the annihilation operators acting on the modes of the sideband frequencies of the central carrier frequency ω_n

$$\hat{a}_n(t) = \int_{-\omega_n}^{\infty} e^{-i\Omega t} \hat{a}_{\Omega} d\Omega, \quad (20)$$

where \hat{a}_{Ω} is the photon annihilation operator in the mode of frequency $\Omega = (\omega - \omega_n)$, Ω represents the sideband frequency and ω_n is the carrier frequency of mode n . Considering a narrow optical spectra for the carrier, $\omega_n \gg |\Omega|$, the integral limit can be approximated as $\omega_n \rightarrow \infty$. In the linearized form, the annihilation operator is can be rewritten as

$$\hat{a}_n(t) = \langle \hat{a}_n \rangle + \delta \hat{a}_n(t) = \alpha_n + \int' e^{-i\Omega t} \hat{a}_{\Omega, n} d\Omega, \quad (21)$$

where α_n represents the mean value of the carrier at frequency ω_n and the symbol $'$ in the integral represents the integration limits between $-\infty$ to ∞ relative to sidebands frequency disregarding the carrier term. This integral will give rise to the fluctuation term $\delta \hat{a}_n(t)$.

The interaction Hamiltonian of each interaction process, Eq. (1) and (2), can now be rewritten with the help of Eq. (21). Higher order terms in fluctuation and rapidly oscillating terms, that don't satisfy energy conservation, are neglected. The constant part having only the mean fields is removed as well. We are left only with the contributions of the sidebands, given by

$$\hat{H}^{(m)} = \int_{\epsilon}^{\infty} d\Omega \hat{H}^{(m)}(\Omega) \quad (22)$$

where the sum is taken form a lower frequency component ϵ defined by the bandwidth of the pump field. The

contributions of the sidebands add linearly, and are described by

$$\begin{aligned} \hat{H}^{(m)}(\Omega) = & i\hbar\chi^{(m)}\Omega[\alpha_0^{*(m-1)}(\hat{a}_{\Omega,1}\hat{a}_{-\Omega,2} + \hat{a}_{-\Omega,1}\hat{a}_{\Omega,2}) \\ & + (m-1)\alpha_0^{*(m-2)}\alpha_1(\hat{a}_{\Omega,0}^{\dagger}\hat{a}_{\Omega,2} + \hat{a}_{-\Omega,0}^{\dagger}\hat{a}_{-\Omega,2}) \\ & + (m-1)\alpha_0^{*(m-2)}\alpha_2(\hat{a}_{\Omega,0}^{\dagger}\hat{a}_{\Omega,1} + \hat{a}_{-\Omega,0}^{\dagger}\hat{a}_{-\Omega,1}) \\ & + (m-2)\alpha_1\alpha_2(\hat{a}_{\Omega,0}^{\dagger}\hat{a}_{-\Omega,0}^{\dagger} + \hat{a}_{-\Omega,0}^{\dagger}\hat{a}_{\Omega,0}^{\dagger}) - h.c.]. \end{aligned} \quad (23)$$

A convenient form of writing this Hamiltonian is using a symmetric and antisymmetric combination of modes, defined as: $\hat{a}_{ns/a} = [\hat{a}_{\Omega, n} \pm \hat{a}_{-\Omega, n}]/\sqrt{2}$, where $+$ ($-$) signal refers to symmetric (antisymmetric) sideband operators thus simplifying the Hamiltonian into two terms, $\hat{H}^{(m)}(\Omega) = \hat{H}_s^{(m)}(\Omega) + \hat{H}_a^{(m)}(\Omega)$, given by:

$$\begin{aligned} \hat{H}_{s/a}^{(m)}(\Omega) = & \pm\alpha_0^{*(m-1)}\hat{a}_{1s/a}\hat{a}_{2s/a} \\ & + (m-1)\alpha_0^{*(m-2)}\alpha_1\hat{a}_{0s/a}^{\dagger}\hat{a}_{2s/a} \\ & + (m-1)\alpha_0^{*(m-2)}\alpha_2\hat{a}_{0s/a}^{\dagger}\hat{a}_{1s/a} \\ & \pm (m-2)\alpha_1\alpha_2\hat{a}_{0s/a}^{\dagger 2} - h.c. \end{aligned} \quad (24)$$

As showed in details in the reference [23], this Hamiltonian represents a two-mode squeezing process on the twin beams in the presence of an intense pump field, and a pair of beam splitter process between the pump and one of the generated fields in the presence of an intense mean field related with the conjugated mode. In the case of Hamiltonian, related to the $\chi^{(3)}$ medium, one additional term is present, which is related with a squeezing process in the pump field in the presence of a pair of intense converted fields.

We can use the Heisenberg equation $d\hat{a}_{n(s/a)}(t)/dt = -i/\hbar[H_{\chi^{(m)}(s/a)}, \hat{a}_{n(s/a)}^{\dagger}(t)]$ to evaluate the transformation of the field operators from the input to the output of the amplifier. Calculation can be performed using an auxiliary variable $\xi_m = \chi^{(m)}t$ giving a compact form for the Heisenberg equation

$$\frac{d\vec{\mathbf{A}}_{(s/a)}}{d\xi_m} = \mathbf{M}_{(s/a)}(\xi_m)\vec{\mathbf{A}}_{(s/a)}, \quad \text{where} \quad (25)$$

$\vec{\mathbf{A}}_{s/a} = (\hat{a}_{0(s/a)} \hat{a}_{0(s/a)}^{\dagger} \hat{a}_{1(s/a)} \hat{a}_{1(s/a)}^{\dagger} \hat{a}_{2(s/a)} \hat{a}_{2(s/a)}^{\dagger})^T$. The evolution matrix has an explicit dependence on the amplitude of the fields inside the crystal, that evolve along the propagation, as evaluated in the previous section,

$$\mathbf{M}_{(s/a)} = \xi_m \begin{pmatrix} 0 & \mp 2(m-2)\alpha_{\omega_1}\alpha_{\omega_2} & -(m-1)\alpha_{\omega_0}^{*(m-2)}\alpha_{\omega_2} & 0 & -(m-1)\alpha_{\omega_0}^{*(m-2)}\alpha_{\omega_1} & 0 \\ \mp 2(m-2)\alpha_{\omega_0}\alpha_{\omega_2}^* & 0 & 0 & -(m-1)\alpha_{\omega_0}^{(m-2)}\alpha_{\omega_2}^* & 0 & -(m-1)\alpha_{\omega_0}^{*(m-2)}\alpha_{\omega_1}^* \\ (m-1)\alpha_{\omega_0}^{(m-2)}\alpha_{\omega_2}^* & 0 & 0 & 0 & 0 & \pm\alpha_{\omega_0}^{m-1} \\ 0 & (m-1)\alpha_{\omega_0}^{*(m-2)}\alpha_{\omega_2} & 0 & 0 & \pm\alpha_{\omega_0}^{m-1} & 0 \\ (m-1)\alpha_{\omega_0}^{(m-2)}\alpha_{\omega_1}^* & 0 & 0 & \pm\alpha_{\omega_0}^{*(m-1)} & 0 & 0 \\ 0 & (m-1)\alpha_{\omega_0}^{*(m-2)}\alpha_{\omega_1} & \pm\alpha_{\omega_0}^{*(m-1)} & 0 & 0 & 0 \end{pmatrix}. \quad (26)$$

Solving the differential Eq. (25), the result can be written as:

$$\vec{\mathbf{A}}_{(s/a)} |_{\xi_m=\kappa^{(m)}} = \mathbf{G}_{m(s/a)} \vec{\mathbf{A}}_{(s/a)} |_{\xi_m=0}, \quad (27)$$

with

$$\mathbf{G}_{m(s/a)} = \exp \left(\int_0^{\kappa^{(m)}} d\xi_m \mathbf{M}_{m(s/a)}(\xi_m) \right). \quad (28)$$

Most of the works until now considered that the evolution of the field inside the crystal is negligible due to the low total power variation of signal of this systems [30], a valid situation for a small gain, typical situation found in closed cavities. The integration of Eq. (28) allows us to study the behavior of the fields inside two different gain media without this consideration enabling the accurate study in the open cavity regime [29].

In order to evaluate the behavior of the field fluctuations in a round trip inside the cavity (Fig. 6) the procedure described in [23] was adapted to a format that can be used considering both $\chi^{(2)}$ and $\chi^{(3)}$ as the gain medium inside the cavity (see Appendix B for further details). The output field $\hat{\mathbf{A}}_{\mathbf{R}}$ from the cavity is directly related to the incident field $\hat{\mathbf{A}}_{\mathbf{in}}$ and the additional vacuum field $\hat{\mathbf{A}}_{\mathbf{v}}$, associated to spurious losses of the cavity, by the relation

$$\vec{\mathbf{A}}_{\mathbf{R}} = \mathbf{R}_{\kappa} \vec{\mathbf{A}}_{\mathbf{in}} + \mathbf{T}_{\kappa} \vec{\mathbf{A}}_{\mathbf{v}}. \quad (29)$$

where \mathbf{R}_{κ} and \mathbf{T}_{κ} are the effective reflection and trans-

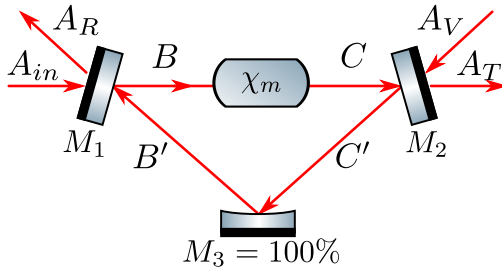


FIG. 6: Representation of the fields inside the cavity with a gain medium $\chi^{(m)}$. M_1 and M_2 are the input and output mirrors, with reflectivities (transmissivities) coefficients \mathbf{R} (\mathbf{T}) and \mathbf{R}' (\mathbf{T}').

mission matrices of the OPO cavity, accounting for all the mirror coupling and the gain transformation described by Eq. (28).

Knowing the OPO output fields, the correlation between the output quadratures can be analyzed. Following the analysis in the reference [23] we performed a complete description of the covariance matrix of the Hermitian operators \hat{p}_{ω_n} and \hat{q}_{ω_n} of pump, signal and idler modes, that satisfies the commutation relation $[\hat{p}_{\omega}, \hat{q}_{\omega'}] = 2i\delta(\omega - \omega')$ and are related with the operators \hat{a}_{ω} and $\hat{a}_{\omega}^{\dagger}$ by $\hat{p}_{\omega} = (\hat{a}_{\omega} + \hat{a}_{\omega}^{\dagger})/2$ and $\hat{q}_{\omega} = i(\hat{a}_{\omega} - \hat{a}_{\omega}^{\dagger})/2$. The covariance matrix of the reflected field is given by:

$$\mathbf{V}_{\mathbf{R}} = \tilde{\mathbf{R}}_{\kappa} \mathbf{V}_{\mathbf{in}} \tilde{\mathbf{R}}_{\kappa}^{-1} + \tilde{\mathbf{T}}_{\kappa} \mathbf{V}_{\mathbf{v}} \tilde{\mathbf{T}}_{\kappa}^{-1}, \quad (30)$$

where $\mathbf{V}_{\mathbf{in}}$ is the input covariance matrix of the pump, signal and idler fields, and $\mathbf{V}_{\mathbf{v}}$ is the covariance matrix related with the input vacuum modes. We considered that the input covariance matrix represents a coherent state, $\mathbf{V}_{\mathbf{v}} = \mathbf{V}_{\mathbf{in}} = \mathbf{I}$. Details of the calculation procedure can be found in [23].

IV. ANALYSIS OF THE COVARIANCE MATRIX

The covariance matrix $\mathbf{V}_{\mathbf{R}}$ gives a unique description of the system, and for a Gaussian state is equivalent to the determination of the density operator [32]. It gives all the possible information about the system, including squeezing and entanglement of the fields. In what follow, we will make a detailed analysis of the quantum features that can be found in the different configurations, DROPO and TROPO, $\chi^{(2)}$ and $\chi^{(3)}$.

In order to give a general view, we have chosen a reflectance of $R = 85\%$ for the output coupler, and no additional loss in the cavity. Analysis frequency is chosen to be half of the cavity bandwidth BW : $\Omega = 0.5(1 - R)/\tau$, where τ is the round trip time of the wave inside the cavity. TROPO is chosen to be with all the reflectances identical.

A. Source of squeezed states

If we want to observe the noise compression, as evaluated for instance in [3], we may restrict the study to

the covariance of the symmetric variables [33]. From the symmetry between signal and idler modes, only the presentation of the variances of one of these fields is necessary. The quadratures associated to the amplitude and phase are represented by Δp_{si} and Δq_{si} , with $i = \{0, 1, 2\}$ for pump, signal and idler fields.

Individual variances for the DROPO are presented in Fig. 7, for $\chi^{(2)}$ and $\chi^{(3)}$ gain medium. Equivalent results for the TROPO are presented in Fig. 8. There are many common features on these curves. The compression of the phase noise of the pump, $\Delta^2 q_{s0}$, as observed in [3], is verified not only in Fig. 8a, but in all the distinct configurations. It is interesting to notice that while the compression is limited to 0.5 in the $\chi^{(2)}$ TROPO [22], the $\chi^{(2)}$ DROPO can beat this value. On the other hand, while compression of this quadrature is presented in $\chi^{(3)}$ OPO, they are not so effective as squeezers for the pump. In fact, for the $\chi^{(3)}$ DROPO, noise compression is even limited to the range of $\sigma < 2.2$. But then we have a curious feature: for $\sigma < 2.3$, the pump amplitude $\Delta^2 p_{s0}$ becomes squeezed. This difference in behavior between $\chi^{(2)}$ and $\chi^{(3)}$ OPOs can be explained by the additional term in Eq. (24), giving the compression operator acting on the pump, associated to the mean converted fields inside the cavity. This effect should compete with the usual dynamics of the phase noise compression provided

by the back conversion of the signal and idler fields into the pump mode described in [3]. For a strong field, it should beat the phase compression.

As for the converted fields, they present a nearly perfect thermal state right above the threshold, but for an increasing pump power, while phase noise $\Delta^2 q_{s1}$ grows smoothly, the amplitude noise $\Delta^2 p_{s1}$ presents a strong peak, that is much more pronounced for the TROPO, and almost coinciding with the peak noise for the pump amplitude $\Delta^2 p_{s0}$. On the other hand, above a certain value, the noise drops and we eventually have noise compression for this field. While this effect was already predicted in the literature for the $\chi^{(2)}$ TROPO, to the best of our knowledge it was not observed yet. A good reason could be the fact that it should appear above $\sigma = 3$, situation where the thermal effects will become dramatic in optical crystals, and the intense fields that are produced will elude the usual homodyne techniques for noise measurement. It would be necessary to use self-homodyning, as done in [8], for its observation. Nevertheless, the use of $\chi^{(3)}$ gain medium on a DROPO reduces the value of the necessary pump power for reaching the squeezed output. In fact, for a $\chi^{(2)}$ DROPO we reach a significant noise reduction to the shot noise level, that was even observed in preliminary studies using an OPO with atomic vapor as the gain medium [29], although squeezing was not yet

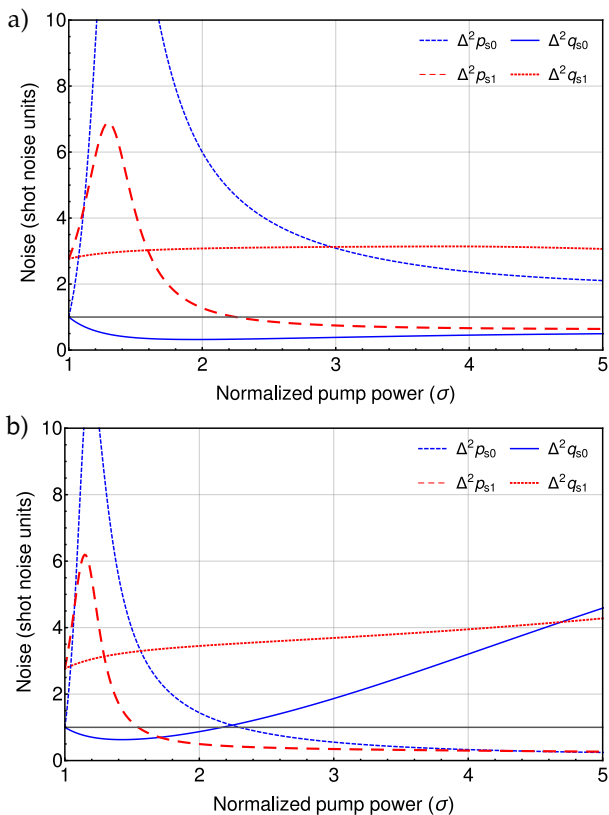


FIG. 7: DROPO: Diagonal terms of V_s in terms of σ for $R_1 = 85\%$ and $\Omega = 0.5BW$. Considering in a) a $\chi^{(2)}$ gain medium and in b) a $\chi^{(3)}$ gain medium.

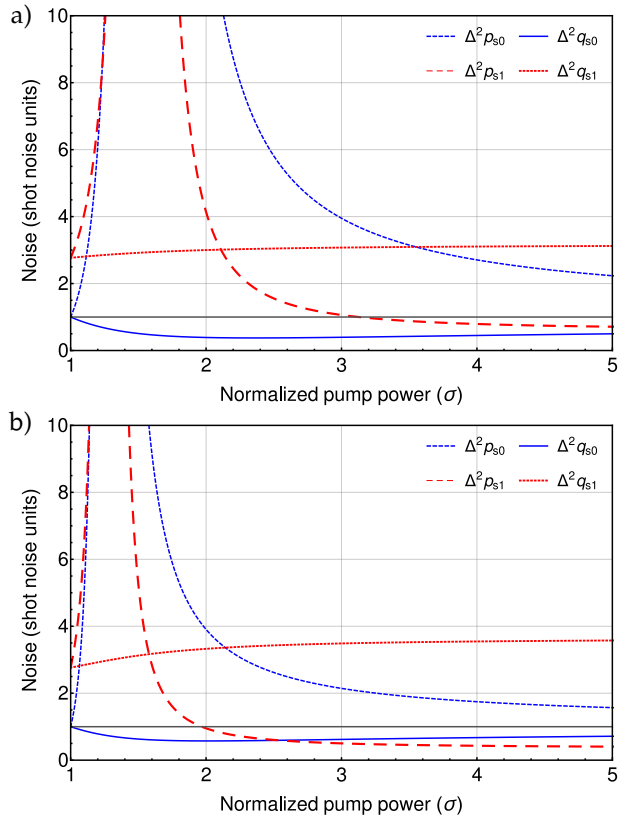


FIG. 8: TROPO: Diagonal terms of V_s in terms of σ for $R_1 = 85\%$ and $\Omega = 0.5BW$. Considering in a) a $\chi^{(2)}$ gain medium and in b) a $\chi^{(3)}$ gain medium.

verified. The strong compression for the amplitudes of pump, signal and idler field is a dramatic demonstration of the role of pump depletion even in a single pass of the beam through the crystal.

B. Bipartite Entanglement

Two mode entanglement, the basic resource for quantum information processing, can be directly observed from the second order momenta [21, 34]. In fact, noise compression in the Einstein-Podolsky-Rosen type operators criteria [34] is a sufficient condition for a successful teleportation of a quantum state between two sites [13]. This DGCZ criterion can be expressed as an inequality of the form

$$\Delta^2 p_- + \Delta^2 q_+ > 2, \quad (31)$$

where the EPR-type variables are $\Delta^2 p_- = (p_{s1} - p_{s2})/\sqrt{2}$ and $\Delta^2 q_+ = (q_{s1} + q_{s2})/\sqrt{2}$. If the variances of these lines combinations of quadratures violates the inequality, the bipartition $\{1, 2\}$ is necessarily entangled.

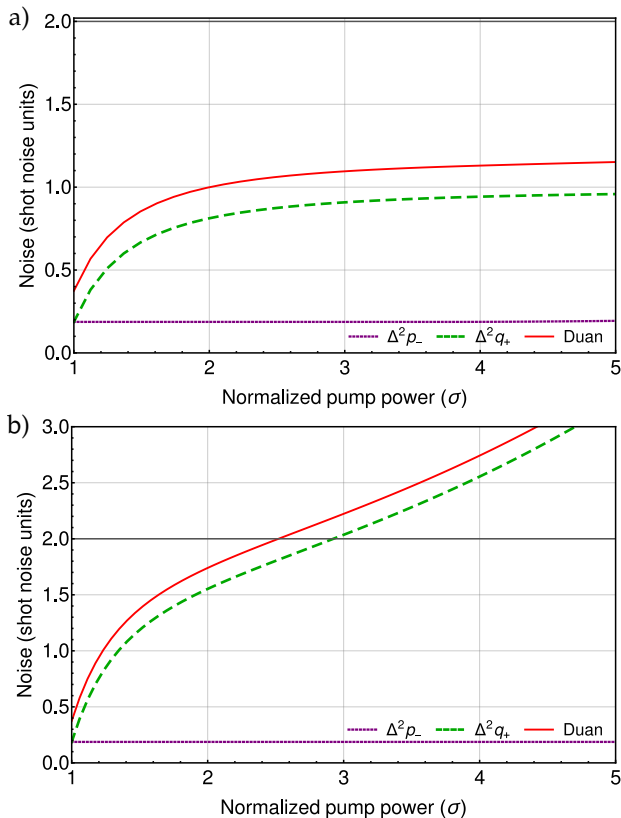


FIG. 9: DROPO: EPR inequality (continuum, orange), $\Delta^2 p_-$ (dashed, purple) and $\Delta^2 q_+$ (dashed, green) in terms of σ for $R_1 = 85\%$ and $\Omega = 0.5BW$. Considering in a) a $\chi^{(2)}$ gain medium and in b) a $\chi^{(3)}$ gain medium. The grey solid line represents the limit value of the inequality given by Eq. (31).

Twin beams produced by OPOs are a regular source of entangled states [6, 8]. In what follows, we will evaluate the noise compression of the correlated intensities and the anti-correlated phases of the fields generated in distinct cavity configurations. Fig. 9 presents the behavior of Eq. (31) considering the DROPO, while Fig. 10 present the results for the TROPO. An outstanding result is the robustness of the twin beam correlation [4]. The subtraction of the amplitudes for all the four configurations is the same, and directly related only to the cavity bandwidth and detection efficiency - the squeezing level depends on the fraction of the twin photons, that are generated by the parametric conversion, that is detected. Therefore, this variance is independent of the pump power, even though the variance of each field may change dramatically, from excess noise to squeezing, as seen in the previous section.

On the other hand, phase anti-correlation, associated to the noise compression in $\Delta^2 q_+$, is more fragile, and depends strongly on the pump power [8]. Starting from the same level as the $\Delta^2 p_-$ close to the threshold, it had a monotonic increase. Here the effect of the gain medium

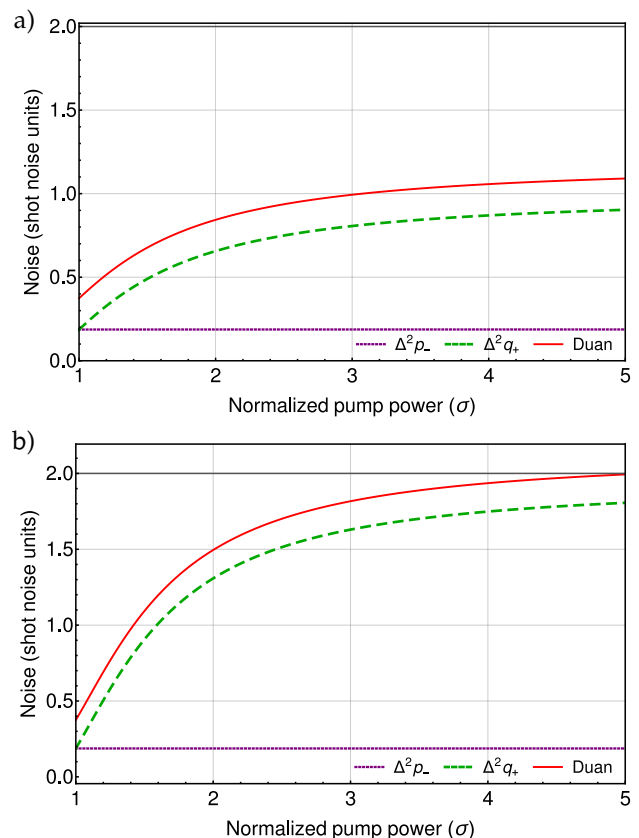


FIG. 10: TROPO: EPR inequality (continuum, orange), $\Delta^2 p_-$ (dashed, purple) and $\Delta^2 q_+$ (dashed, green) in terms of σ for $R_1 = 85\%$ and $\Omega = 0.5BW$. Considering in a) a $\chi^{(2)}$ gain medium and in b) a $\chi^{(3)}$ gain medium. The grey solid line represents the limit value of inequality Eq. (31).

is very relevant: while $\chi^{(2)}$ OPOs have a limit where this variance asymptotically reaches the vacuum level for increasing pump power ($\Delta^2 q_+ < 1$), $\chi^{(3)}$ OPOs will cross this limit at very low pump power, $\sigma \simeq 1.5$. Moreover, the loss of noise compression for growing pump power is more pronounced in the DROPOs, when compared to TROPOs, for both gain medium, and should be considered on the development of entangled bipartite sources.

As a result, DGCZ inequality is violated for all the value range for the $\chi^{(2)}$ OPOs, but it is satisfied only up to a certain level of pump power for $\chi^{(3)}$ OPOs. This is a main limitation of this system for bipartite entanglement, but since we are dealing here with pure states, the loss of entanglement in this two mode partition can be understood as their coupling to other modes of the system, as we should see in the next subsection.

Another important analysis is related with the behavior of the noise spectrum in terms of the analysis frequency normalized by the cavity bandwidth Ω_{BW} . As an example, we focus on the subtraction of the signal and idler fields. It is very well known that in $\chi^{(2)}$ OPOs the behavior of the phase ($\Delta^2 q_{s-}$) and amplitude ($\Delta^2 p_{s-}$) are insensitive to the pump power, and depends only on the analysis frequency. Noise compression in $\Delta^2 p_{s-}$ will follow a Lorentzian, of width given by the cavity bandwidth, and for a lossless system, we have $\Delta^2 p_{s-} \Delta^2 q_{s-} = 1$. The same situation is verified for the DROPO, as can be observed in Fig. 11. This response was recently been observed for a $\chi^{(3)}$ DROPO with atomic vapor [29], where the twin beam generation has showed to be independent of the pump power, and follow a Lorentzian shape.

C. Tripartite Entanglement

While DGCZ criterion is a useful test for bipartite entanglement, it is not both necessary and sufficient on its usual form (Eq. 31). On the other hand, positivity under partial transposition (PPT) was showed to be a necessary and sufficient criterion not only for bipartite Gaussian states [32], but for $1 \times N$ bipartitions as well [35].

Partial transposition operation in a CV system is like a mirror reflection in the phase space, acting only in a partition. When a transposition operator is applied on the density operator, the corresponding Wigner function transforms as $W(\mathbf{x}) \rightarrow W(\mathbf{\Gamma}\mathbf{x})$, with $\mathbf{x} = (p_1, q_1, p_2, q_2)$, we have the substitution of $\mathbf{x} \rightarrow \mathbf{\Gamma}\mathbf{x}$, with $\mathbf{\Gamma} = \text{diag}(1, 1, 1, -1)$. If the new Wigner function does not correspond to physical density operator, the system is entangled. On the other hand, if it does and the Wigner function is Gaussian, then we know that the bipartition is separable, PPT can be immediately verified by the covariance matrix. Writing the set of commutation rules as $[\hat{x}_i, \hat{x}_j] = i\Omega_{i,j}$ where $\Omega = \bigoplus_{k=1}^N J$ and $J = \begin{pmatrix} 0 & 1 \\ -1 & 0 \end{pmatrix}$, the uncertainty relation can be expressed

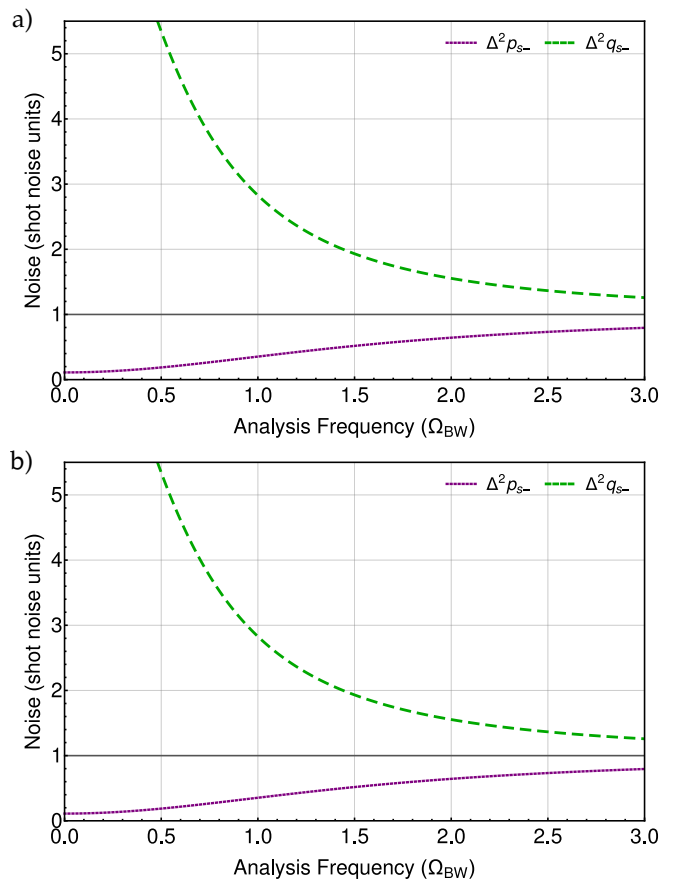


FIG. 11: DROPO: $\Delta^2 p_{s-}$ and $\Delta^2 q_{s-}$ in terms of Ω (normalized by the cavity bandwidth BW) for $R_1 = 85\%$ and $\Omega_{BW} = 0.5$. Considering in a) a $\chi^{(2)}$ gain medium and in b) a $\chi^{(3)}$ gain medium.

as $\mathbf{V} + i\Omega \geq 0$. Partial transposition implies in the transformation $\mathbf{V} \xrightarrow{PT} \tilde{\mathbf{V}} = \mathbf{\Gamma}\mathbf{V}\mathbf{\Gamma}$. Physicality of the partially transposed covariance, $\tilde{\mathbf{V}} + i\Omega \geq 0$, can be verified by the evaluation of the symplectic eigenvalues ν_k of $\tilde{\mathbf{V}}$ [36–38].

$$\nu_k = \sqrt{[\text{Eigenvalues}(\mathcal{V})]_k}, \quad (32)$$

where $\mathcal{V} = -(\tilde{\mathbf{V}}\Omega)^2$. When $\nu_k \geq 1 \forall k$ the transformed matrix $\tilde{\mathbf{V}}$ is physical. It follows from this conditions that if the minimum symplectic eigenvalue $\nu < 1$, the covariance matrix \mathbf{V} corresponds to an entangled state, and the minimum symplectic eigenvalue is an entanglement witness for the given bipartition. The treatment can be extended to multipartite states, and for a $1 \times N$ bipartition, this is a necessary and sufficient condition to demonstrate entanglement for Gaussian states [35].

For this subsection, we will keep our analysis on the subspace of the symmetric covariance matrix, as it will reflect the kind of entanglement usually observed when each beam issued from the OPO is treated as a single mode [9]. For three modes, we have three possible bipar-

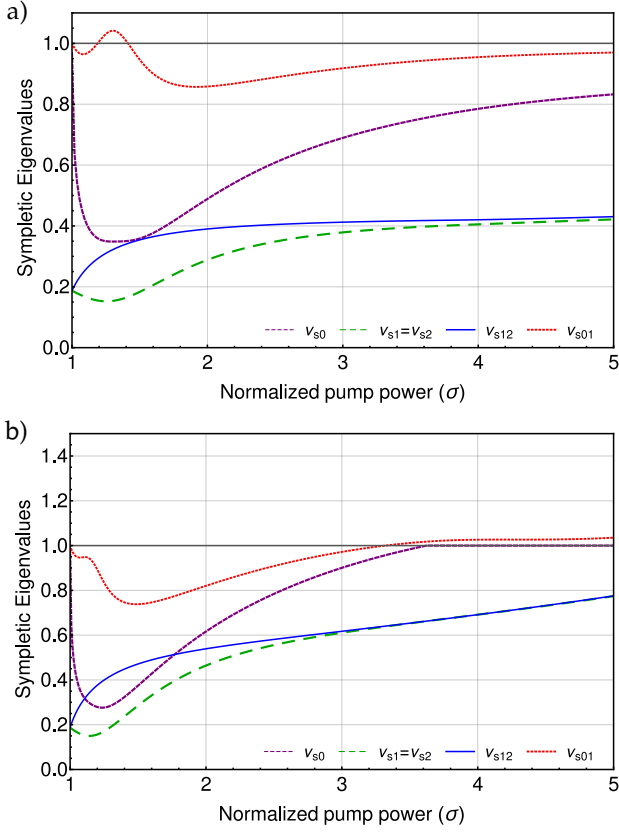


FIG. 12: DROPO: Minimum symplectic eigenvalues ν_k obtained from \mathbf{V}_s in terms of σ for $R_1 = 85\%$ and $\Omega = 0.5BW$. Considering in a) a $\chi^{(2)}$ gain medium and in b) a $\chi^{(3)}$ gain medium. The grey solid line represents the limit value of Eq. (32).

titions 1×2 and the tripartite entanglement is verified if $\nu < 1$ for all of them. Since the Simon-PPT criteria is necessary and sufficient, we will apply it as well to the subsystems formed by pairs of the beams, comparing the conclusions to those inferred from the DGCZ criterion.

In Figs. 12 and 13 the behavior of the symplectic eigenvalues for the DROPO and TROPO are presented. For three modes, we have the eigenvalue for the transposition of the pump, ν_0 , and for signal or idler, $\nu_1 = \nu_2$. We plot the transposition for the possible two mode subsystems, for pump and signal (or idler) $\nu_{01} = \nu_{02}$ and the pair formed by the converted fields ν_{12} .

It is evident that entanglement of each converted mode to the rest of the system is always verified (ν_1), but the violation is reduced for increasing pump power. It is consistent with the fact that the converted fields are strongly entangled, as can be seen by ν_{12} . If you compare this situation with the observed in Figs. 9 and 10, it is clear that Eq. (31) fails in identifying some entangled states: as stated in [34], the condition is both necessary and sufficient only if the covariance matrix is in one of the standard form that they propose in the article. But a feature is common in both witnesses: the violation for the $\chi^{(3)}$ DROPO is rapidly reduced for a growing pump

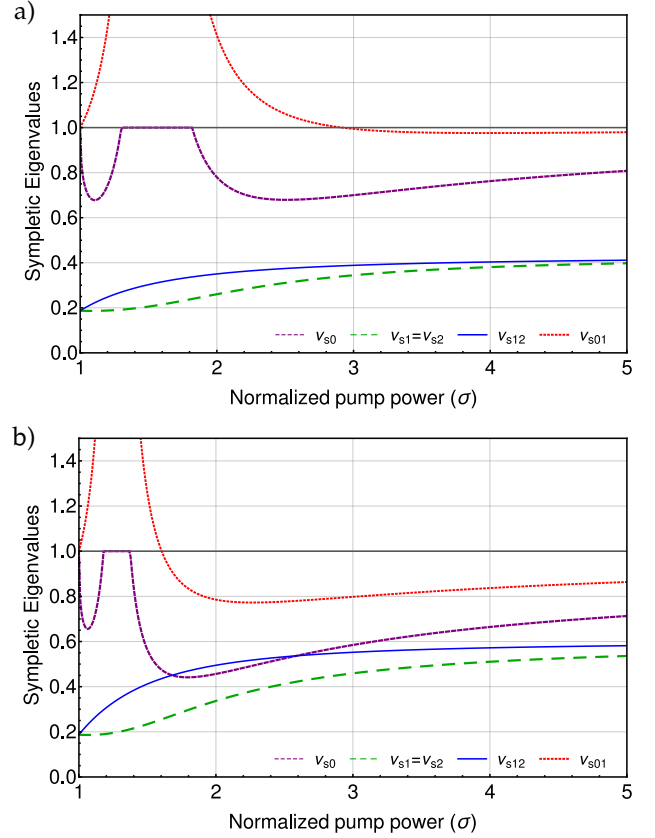


FIG. 13: TROPO: Minimum symplectic eigenvalues ν_k obtained from \mathbf{V}_s in terms of σ for $R_1 = 85\%$ and $\Omega = 0.5BW$. Considering in a) a $\chi^{(2)}$ gain medium and in b) a $\chi^{(3)}$ gain medium. The grey solid line represents the limit value of Eq. (32).

power.

Situation is more peculiar when we look at the pump mode. Entanglement of the pump with the pair of the converted fields ν_0 , or with just one of the fields ν_{01} is weaker than the observed for each of the down converted beams. Moreover, it can vanish in the region where we observe the peak in the amplitude fluctuations in Figs. 7 and 8. This apparent loss of entanglement is not observed in other configurations of the TROPO [9, 39], where it remains entangled over the entire span of the pump power. The main difference in this case is the fact that all the modes have the same loss for the cavity. This loss of entanglement would be expected if we have loss of purity in the tripartite state [40], but as we have found, the situation is more subtle, and looking in the details of the sideband modes, we have in fact hexapartite entanglement on the system [10]. As for the $\chi^{(3)}$ DROPO, we can see that for sufficiently high pump power the pump is apparently disentangled from the twin pair. That is not necessarily true, if we consider now the correlation between the symmetric and the antisymmetric part of the covariance matrix.

D. Multipartite entanglement

So far, we have limited our analysis only to the symmetric combination of the sidebands, that was showed to be equivalent to the antisymmetric part [33] in the OPO. As we have showed in [10], in the TROPO all the possible 31 bipartitions are entangled. Therefore, we will restrict the current analysis to the relevant features involving bipartitions in the symmetric/antisymmetric basis

For the six modes involved, we will explore the bipartition involving all the modes of the pump (ν_{s0a0}) and all the modes of the signal or idler ($\nu_{s1a1} = \nu_{s2a2}$). It will also be relevant to explore the $\times 3$ partition, involving all the symmetric \times all the antisymmetric modes (ν_{sa}).

As we can see in Figs. 14 (for the DROPO) and 15 (for the TROPO), entanglement for the pump is completely recovered once we account for the complete description of the state. The same is true for signal or idler modes. The reason for this effect is clear when we consider the shared information between symmetric and antisymmetric case:

entanglement is maximized, with a particularly strong violation for ν_{sa} in the TROPO (Fig. 15). We have a minimum of ν_{sa} in the region where we have a peak in the noise of the amplitudes (Figs. 7 and 8). This peak is associated with a strong correlation between the symmetric and antisymmetric modes, as is showed in the Appendix C. This effect is dramatically enhanced in the TROPO when the three modes have balanced losses, and is less dramatic (yet still recognizable [33]) for the usual $\chi^{(2)}$ TROPO, where the coupling of the cavity for the pump is ≈ 5 times that of the downconverted modes. On the other hand, for the χ^3 OPO, we have a unitary value for ν_{sa} , at $\sigma = 2$ for the DROPO and $\sigma = 4$ for the TROPO. That is associated to a vanishing correlation between the partitions, as can be seen in Appendix C.

Finally, instead of considering the bipartite case of pump and idler, or signal and idler, we may now consider the whole symmetric and antisymmetric combination for the pair of beams. We may compare now ν_{sa12} in Figs. 14 and 15 with ν_{s12} in Figs. 7 and 8. We can-

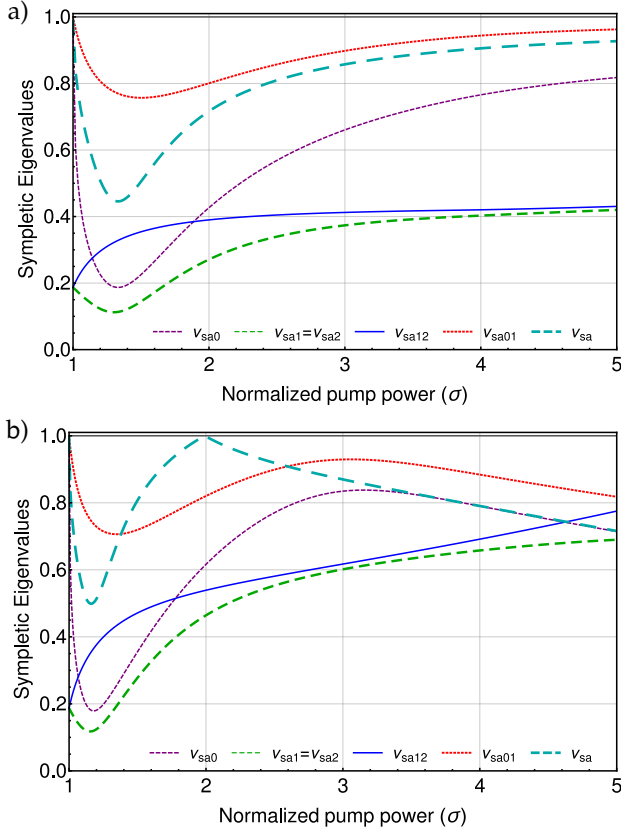


FIG. 14: DROPO: Minimum symplectic eigenvalues $\nu_{sa,k}$ considering $\mathbf{V}_{s/a}$ in terms of σ for $R_1 = 85\%$ and $\Omega_{BW} = 0.5$. $k = \{0, 1, 01, 12\}$ represent the subsystems of pump, signal, pump and signal, signal and idler fields respectively, and ν_{sa} is obtained by the transposition of antisymmetric pump, signal and idler fields. Considering in a) a $\chi^{(2)}$ gain medium and in b) a $\chi^{(3)}$ gain medium.

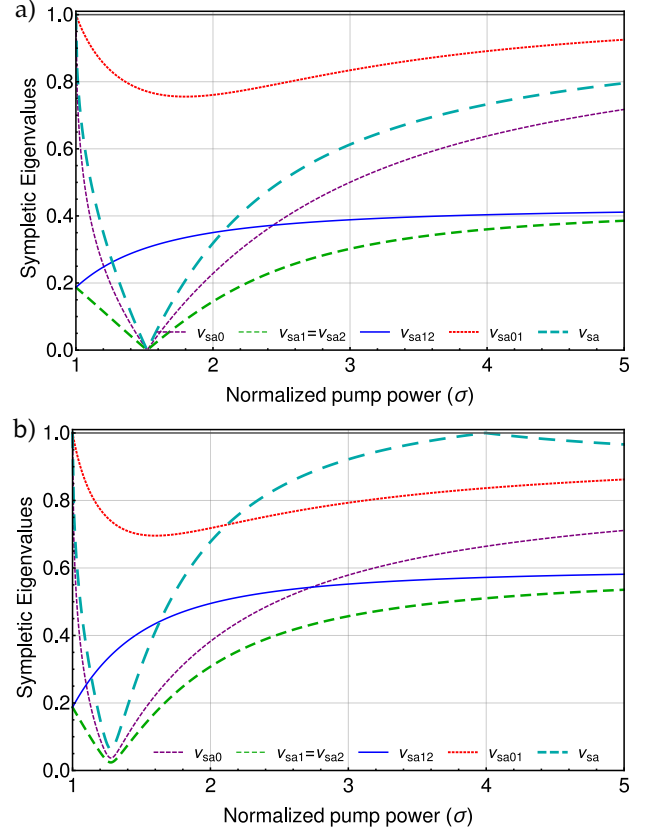


FIG. 15: TROPO: Minimum symplectic eigenvalues $\nu_{sa,k}$ considering $\mathbf{V}_{s/a}$ in terms of σ for $R_1 = 85\%$ and $\Omega_{BW} = 0.5$. In which $k = \{0, 1, 01, 12\}$ represent the subsystems of pump, signal, pump and signal, signal and idler fields respectively, and ν_{sa} is obtained by the transposition of antisymmetric pump, signal and idler fields. Considering in a) a $\chi^{(2)}$ gain medium and in b) a $\chi^{(3)}$ gain medium.

not observe any difference, what is consistent with the absence of correlation between symmetric and antisymmetric part for signal and idler subsystems. That is not true for the pump mode, that presents relevant correlations involving the symmetric and antisymmetric part of the signal (or idler) modes as can be observed from ν_{sa01} in Figs. 14 and 15 compared to ν_{s01} in Figs. 7 and 8. Entanglement between pump and signal in this case is recovered once that the correlation between symmetric and antisymmetric part are taken into account.

V. CONCLUSION

We can see clearly that the versatility of the OPO as a source of non-classical states in the continuous variable regime is not an exclusivity of the PDC process, but is also present in the case of $\chi^{(3)}$ media. Moreover, even for an extremely open cavity, reaching the limit of a single-pass of the pump through the amplifier, as is the case of the DROPO, noise compression and pump entanglement are also present. The method presented in [23] we have successfully employed reproduces these features observed in the TROPO, and put in evidence the similarities of the DROPO in comparison with the TROPO.

Our analysis here is quite distinct from the one performed for the TROPO in [10, 23], that focus on the role of individual sidebands of each one of the beams. In our current approach, we kept the analysis for six modes, but heading back to the symmetric/antisymmetric basis of these sidebands. The reason is twofold: that is the usual measurement basis, leading to the image of entanglement involving individual beams (considered as carrier plus sidebands), and gives a greater evidence of the role of the correlations between the symmetric and antisymmetric spaces. Although identical in individual information, they share a strong correlation leading to relevant entanglement. A good amount of information is lost if this correlation is ignored.

This fact is particularly evident for the dynamics of a cavity with equal losses for the pump, signal and idler, and we can in this case observe the dramatic effect of the entanglement between the symmetric and the antisymmetric modes. It makes a clear difference between the tripartite case and the hexapartite analysis. We may conclude that a detailed analysis of the sidebands is much more than just a reproduction of two equivalent tripartite systems, but rather a rich system of six strongly entangled modes.

While the parametric amplification in the single pass regime [27] can provide strong correlations in the 4WM process, the use of a cavity can provide a great enhancement of these effects: the twin beam correlation can be as perfect as the ratio of the coupling to the overall losses of the cavity approaches unit. In this case, open cavities, as showed in [29], are a promising source of entangled states.

The linear treatment presented here can give further guidance for the transition between the two operational regimes. It is expected that the linearization should fail close to the oscillation threshold [41]. If that is the case, we may go beyond the treatment described in Eq. (22), that gives only bi-linear operators, that keep the Gaussianity of the input states. But with open cavities, thanks to the high gain, this sudden transition may be smoother and a detailed investigation of the evolution of the state, with the measurement of higher order momenta, could be performed.

VI. ACKNOWLEDGMENTS

BAFR and RBA contributed equally for the present work. We thank C. Gonzalez-Arciniegas and P. Nussenzeig for fruitful discussions. This work was supported by FAPESP proc. 2015/18834-0, CAPES and CNPq. B. M. is supported by FAPESP proc. 2014/27223-2.

-
- [1] J. A. Giordmaine and R. C. Miller. Tunable coherent parametric oscillation in *linbo3* at optical frequencies. *Phys. Rev. Lett.*, 14(24):973, 1965.
 - [2] Ling-An Wu, H. J. Kimble, J. L. Hall, and Huifa Wu. Generation of squeezed states by parametric down conversion. *Phys. Rev. Lett.*, 57:2520–2523, Nov 1986.
 - [3] K. Kasai, Gao Jiangrui, and C. Fabre. Observation of squeezing using cascaded nonlinearity. *Europhysics Letters*, 40:25, 1997.
 - [4] A. Heidmann, R. J. Horowicz, S. Reynaud, E. Giacobino, C. Fabre, and G. Camy. Observation of quantum noise reduction on twin laser beams. *Phys. Rev. Lett.*, 59:2555–2557, Nov 1987.
 - [5] K. N. Cassemiro, A. S. Villar, P. Valente, M. Martinelli, and P. Nussenzeig. Experimental observation of three-color optical quantum correlations. *Opt. Lett.*, 32(6):695–697, Mar 2007.
 - [6] Z. Y. Ou, S. F. Pereira, H. J. Kimble, and K. C. Peng. Realization of the einstein-podolsky-rosen paradox for continuous variables. *Phys. Rev. Lett.*, 68:3663, 1992.
 - [7] C. Schori, J. L. Sørensen, and E. S. Polzik. Narrow-band frequency tunable light source of continuous quadrature entanglement. *Phys. Rev. A*, 66:033802, 2002.
 - [8] A. S. Villar, L. S. Cruz, K. N. Cassemiro, M. Martinelli, and P. Nussenzeig. Generation of bright two-color continuous variable entanglement. *Phys. Rev. Lett.*, 95:243603, 2005.
 - [9] A. S. Coelho, F. A. S. Barbosa, K. N. Cassemiro, A. S. Villar, M. Martinelli, and P. Nussenzeig. Three-color entanglement. *Science*, 326(5954):823–826, 2009.
 - [10] F. A. S. Barbosa, A. S. Coelho, L. F. Muñoz-Martínez, L. Ortiz-Gutiérrez, A. S. Villar, P. Nussenzeig, and M. Martinelli. Hexapartite entanglement in an above-threshold optical parametric oscillator. *Phys. Rev. Lett.*,

- 121(7):073601, 2018.
- [11] H. Vahlbruch, S. Chelkowski, K. Danzmann, and R. Schnabel. Quantum engineering of squeezed states for quantum communication and metrology. *New Journal of Physics*, 9(10):371, 2007.
- [12] S. F. Pereira, Z. Y. Ou, and H. J. Kimble. Quantum communication with correlated nonclassical states. *Phys. Rev. A*, 62:042311, 2000.
- [13] A. Furusawa, J. L. Sørensen, S. L. Braunstein, C. A. Fuchs, A. Christopher, H. J. Kimble, and E. S. Polzik. Unconditional quantum teleportation. *Science*, 282(5389):706–709, 1998.
- [14] S. Yokoyama, R. Ukai, and et al. S. Armstrong. Ultra-large-scale continuous-variable cluster states multiplexed in the time domain. *Nature Photon.*, 7:982, 2013.
- [15] Moran Chen, N. C. Menicucci, and O. Pfister. Experimental realization of multipartite entanglement of 60 modes of a quantum optical frequency comb. *Phys. Rev. Lett.*, 112:120505, 2014.
- [16] C Mile Gu, Weedbrook, N. C. Menicucci, T. C. Ralph, and P. van Loock. Quantum computing with continuous-variable clusters. *Phys. Rev. A*, 79, 2009.
- [17] J. A. Giordmaine. Mixing of light beams in crystals. *Phys. Rev. Lett.*, 8(1):19, 1962.
- [18] C. Fabre, P. F. Cohadon, and C. Schwob. Cw optical parametric oscillators: single mode operation and frequency tuning properties. *Quantum Semiclass. Opt.*, 9:165, 1997.
- [19] R. Graham and H. Haken. The quantum-fluctuations of the optical parametric oscillator. i. *Zeitschrift für Physik A Hadrons and nuclei*, 210(3):276–302, 1968.
- [20] P. D. Drummond and M. D. Reid. Correlations in non-degenerate parametric oscillation. ii. below threshold results. *Phys. Rev. A*, 41(7):3930, 1990.
- [21] M. D. Reid and P. D. Drummond. Correlations in non-degenerate parametric oscillation: Squeezing in the presence of phase diffusion. *Phys. Rev. A*, 40:4493, 1989.
- [22] C Fabre, E Giacobino, A Heidmann, L Lugiato, S Reynaud, M Vadamchino, and Wang Kaige. Squeezing in detuned degenerate optical parametric oscillators. *Quantum Optics: Journal of the European Optical Society Part B*, 2(2):159–187, apr 1990.
- [23] L. F. Muñoz Martínez, F. A. S. Barbosa, A. S. Coelho, L. Ortiz-Gutiérrez, M. Martinelli, P. Nussenzeig, and A. S. Villar. Exploring six modes of an optical parametric oscillator. *Phys. Rev. A*, 98:023823, Aug 2018.
- [24] B. Yurke. Use of cavities in squeezed-state generation. *Phys. Rev. A*, 29:408(R), 1984.
- [25] B. Yurke. Squeezed-coherent-state generation via four-wave mixers and detection via homodyne detectors. *Phys. Rev. A*, 32, 1985.
- [26] T. J. Kippenberg, S. M. Spillane, and K. J. Vahala. Kerr-nonlinearity optical parametric oscillation in an ultrahigh-q toroid microcavity. *Phys. Rev. Lett.*, 93:083904, 2004.
- [27] C. F. McCormick, A. M. Marino, V. Boyer, and P. D. Lett. Strong low-frequency quantum correlations from a four-wave-mixing amplifier. *Phys. Rev. A*, 78:043816, Oct 2008.
- [28] Xudong Yu, Min Xiao, and Jing Zhang. Triply-resonant optical parametric oscillator by four-wave mixing with rubidium vapor inside an optical cavity. *Appl. Phys. Lett.*, 96(4):041101, 2010.
- [29] A. Monta na Guerrero, M. Martinelli, A. M. Marino, and H. M. Florez. Quantum noise correlations of an optical parametric oscillator based on a non-degenerate four wave mixing process in hot alkali atoms. *arXiv:2004.01590*, 2020.
- [30] T. Debuisschert, A. Sizmann, E. Giacobino, and C. Fabre. Type-ii continuous-wave optical parametric oscillators: oscillation and frequency-tuning characteristics. *J. Opt. Soc. Am. B*, 10(9):1668–1680, Sep 1993.
- [31] E. Rosencher and C. Fabre. Oscillation characteristics of continuous-wave optical parametric oscillators: beyond the mean-field approximation. *J. Opt. Soc. Am. B*, 19(5):1107–1116, 2002.
- [32] R. Simon. Peres-horodecki separability criterion for continuous variable systems. *Phys. Rev. Lett.*, 84:2726, 2000.
- [33] F. A. S. Barbosa, A. S. Coelho, K. N. Cassemiro, P. Nussenzeig, C. Fabre, A. S. Villar, and M. Martinelli. Quantum state reconstruction of spectral field modes: Homodyne and resonator detection schemes. *Phys. Rev. A*, 88:052113, Nov 2013.
- [34] Lu-Ming Duan, G. Giedke, J. I. Cirac, and P. Zoller. Inseparability criterion for continuous variable systems. *Phys. Rev. Lett.*, 84:2722–2725, Mar 2000.
- [35] R. F. Werner and M. M. Wolf. Bound entangled gaussian states. *Phys. Rev. Lett.*, 86:3658, 2001.
- [36] Gerardo Adesso and Fabrizio Illuminati. Entanglement in continuous-variable systems: recent advances and current perspectives. *Journal of Physics A: Mathematical and Theoretical*, 40(28):7821, 2007.
- [37] Gerardo Adesso. *Entanglement of Gaussian States*. PhD thesis, Universit degli Studi di Salerno, 2006.
- [38] John Williamson. On the algebraic problem concerning the normal forms of linear dynamical systems. *American Journal of Mathematics*, 1936.
- [39] A. S. Villar, M. Martinelli, C. Fabre, and P. Nussenzeig. Direct production of tripartite pump-signal-idler entanglement in the above-threshold optical parametric oscillator. *Phys. Rev. Lett.*, 97:140504, 2006.
- [40] T. Golubeva, Yu. Golubev, C. Fabre, and N. Treps. Quantum state of an injected tropo above threshold: purity, glauber function and photon number distribution. *The European Phys. Journal D*, 46:179, 2008.
- [41] K. Dechoum, M. D. Hahn, R. O. Vallejos, and A. Z. Khoury. Semiclassical wigner distribution for a two-mode entangled state generated by an optical parametric oscillator. *Phys. Rev. A*, 81:043834, 2010.

Appendix A: TROPO with different reflection coefficients

An explicit procedure to evaluate the output of a $\chi^{(3)}$ TROPO, P_{1out} , as a function of P_{0in} , R_0 and R_1 can begin by expressing the total photon number, P_{T0} , as a function of those parameters. By taking the square of Eq. (13) and replacing $P_0(L) = P_0(0) - 2\Delta P_1^{(3)}$ considering that $\Delta P_1^{(3)} = P_1(0)(1 - R_1)/R_1$ in Eq. (11), we end up with:

$$4T_0R_0P_{0in} \left(P_0(0) - 2\frac{1-R_1}{R_1}P_1(0) \right) = \quad (A1)$$

$$\left(-T_0P_{0in}(0) + P_0(0) + 2R_0(0)\frac{1-R_1}{R_1}P_1(0) \right)^2.$$

Now, we replace $P_1(0) = (P_{T0} - P_0(0))/2$ and rearranging the result relating $P_0(0)$, P_{T0} and P_{0in} we have

$$4R_1T_0R_0(0)P_{0in} (P_0(0) - (1 - R_1)P_{T0}) = \quad (A2)$$

$$((R_1 - R_0)P_0(0) + R_0P_{T0}(1 - R_1) - R_1P_{0in}(1 - R_0))^2.$$

Solution of Eq. (A2) for $P_0(0)$ leads to two distinct results. We substitute those results in equation $P_1(0) = (P_{T0} - P_0(0))/2$ and we find two possible solutions for $P_1(0)$.

From these two possible results, we can numerically find two solutions for P_{T0} for a given P_{0in} . As an example, Fig. 16 shows those two solutions behave for $R_0 = 0.95$ and $R_1 = 0.80$. Since $P_{T0} > 0$ for $P_{0in} > 0$, the second solution can be discarded, and just the first one is used for the evaluation of the output fields, feeding back the values into Eqs. (8) and (11).

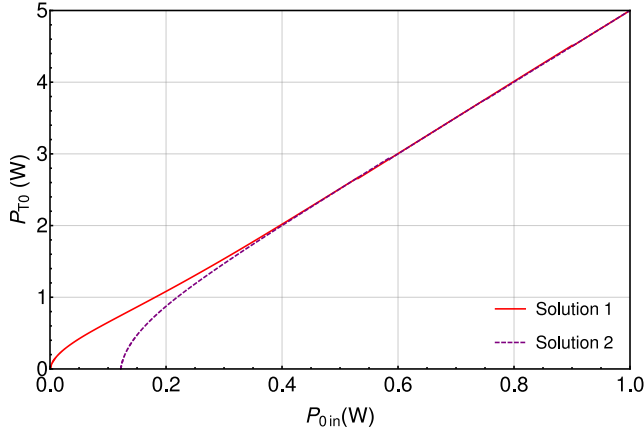


FIG. 16: P_{T0} as a function of P_{0in} . Solution 1 and Solution 2 are the results of $P_{T0}(P_{0in})$ when you carry the calculation with each of the two roots of $P_0(0)$.

We present the output power of the TROPO considering different possibilities for R_0 (75%, 85% and 95%) while keeping $R_1 = 95\%$ fixed. In Fig. 17a we present the model used in [30] for a $\chi^{(2)}$ TROPO, that it is a

widely used description, for comparison with the results of Fig. 17b, where we present the $\chi^{(3)}$ TROPO output power behavior. One can notice that the curve deviates from the parabolic response for $\chi^{(2)}$ media, but as in Fig. 4, the qualitative behavior is similar.

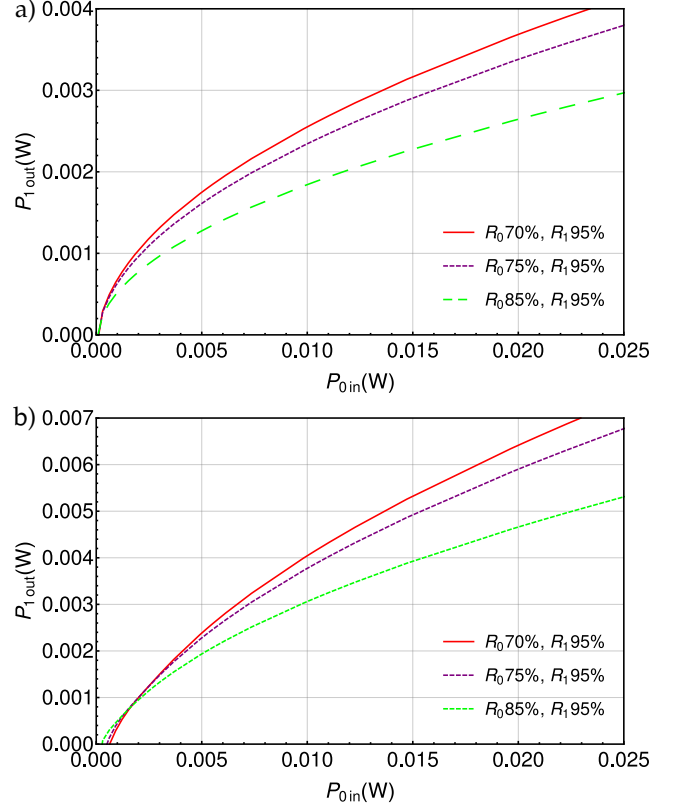


FIG. 17: TROPO $R_1 \neq R_0$. P_{1out} in function of P_{0in} for different reflectivity coefficients $R_0 = \{75\%, 85\%, 95\%\}$ and $R_1 = 75\%$. a) $\chi^{(2)}$ TROPO b) $\chi^{(3)}$ TROPO.

Appendix B: Input-output relations in the open cavity

The explicit derivation of Eq. (29), following the system described in Fig. 6, follows the description presented in [23]. The coupling mirror has reflection and transmission coefficients $r_n = \sqrt{R_n}$ and $t_n = \sqrt{1 - R_n}$ for each carrier, and we assume that one of the mirror as a reflection coefficient r'_n and transmission coefficient t'_n accounting for spurious losses. The equations relating each field operator inside and outside the cavity are given by the beam splitter transformations

$$\vec{A}_R = R\vec{A}_{in} + T\vec{B}', \quad \vec{B} = T\vec{A}_{in} - R\vec{B}', \quad (B1)$$

$$\vec{A}_T = R'\vec{A}_\nu + T'\vec{C}, \quad \vec{C}' = T'\vec{A}_\nu - R'\vec{C}, \quad (B2)$$

with

$$\begin{aligned}\mathbf{R} &= \text{diag}(r_0 \ r_0 \ r_1 \ r_1 \ r_2 \ r_2 \ r_0 \ r_0 \ \cdots), \\ \mathbf{T} &= \text{diag}(t_0 \ t_0 \ t_1 \ t_1 \ t_2 \ t_2 \ t_0 \ t_0 \ \cdots), \\ \mathbf{R}' &= \text{diag}(r'_0 \ r'_0 \ r'_1 \ r'_1 \ r'_2 \ r'_2 \ r'_0 \ r'_0 \ \cdots), \\ \mathbf{T}' &= \text{diag}(t'_0 \ t'_0 \ t'_1 \ t'_1 \ t'_2 \ t'_2 \ t'_0 \ t'_0 \ \cdots),\end{aligned}\quad (\text{B3})$$

with the vector fields changed from the symmetric/antisymmetric basis into the basis of the sideband operators $\vec{\mathbf{A}} = (\hat{a}_{\omega_0+\Omega}^{(0)} \ \hat{a}_{\omega_0+\Omega}^{(0)\dagger} \ \cdots \ \hat{a}_{\omega_0-\Omega}^{(0)} \ \hat{a}_{\omega_0-\Omega}^{(0)\dagger} \ \cdots)^T$.

The round trip of the fields inside the cavity will account for both parametric gain \mathbf{G}' (Eq. 27, properly transformed into the sideband mode basis) and additional phase, leading to the transformation

$$\vec{\mathbf{C}} = e^{-i\varphi} \mathbf{G}' \vec{\mathbf{B}}, \quad \vec{\mathbf{B}}' = e^{-i\varphi} \mathbf{G}' \vec{\mathbf{C}}'. \quad (\text{B4})$$

The phase vector

$$\varphi = \varphi(\Omega) \oplus \varphi(-\Omega), \quad (\text{B5})$$

with,

$$\varphi(\Omega) = \text{diag}(\varphi_{\Omega}^{(0)}, -\varphi_{\Omega}^{(0)}, \varphi_{\Omega}^{(1)}, -\varphi_{\Omega}^{(1)}, \varphi_{\Omega}^{(2)}, -\varphi_{\Omega}^{(2)}),$$

gives a different contribution for each sideband depending of the frequency shift Ω

$$\varphi_{\Omega}^{(n)} = \frac{\Omega}{2 \text{FSR}_n}. \quad (\text{B6})$$

where we consider exact resonance of the carrier mode and $\text{FSR}_n = c/2L$ as the free spectral range for the mode n .

Combining beam splitter transformation, phase evolution and gain, expressed in Eqs.(B1–B4) we obtain the linear transformation, Eq. 29 with the coupling matrices given by

$$\mathbf{R}_{\chi} = \mathbf{R} - \mathbf{T} e^{-i\varphi} \mathbf{G}(\chi) \mathbf{R}' e^{-i\varphi} \mathbf{G}(\chi) \mathbf{D}(\chi) \mathbf{T}, \quad (\text{B7})$$

$$\mathbf{T}'_{\chi} = \mathbf{T} e^{-i\varphi} \mathbf{G}(\chi) [\mathbf{I} + \mathbf{R}' e^{-i\varphi} \mathbf{G}(\chi) \mathbf{D}(\chi) \mathbf{R} e^{-i\varphi} \mathbf{G}(\chi)] \mathbf{T}', \quad (\text{B8})$$

and

$$\mathbf{D}(\chi) = \left(\mathbf{1} - \mathbf{R} e^{-i\varphi} \mathbf{G}(\chi) \mathbf{R}' e^{-i\varphi} \mathbf{G}(\chi) \right)^{-1}, \quad (\text{B9})$$

with special care in the basis transformation, from the sideband description (useful for phase propagation given by Eq. B6) to the symmetric/antisymmetric combination (useful for parametric gain given by Eq. 27), as done in [23].

Appendix C: Correlations between symmetric and antisymmetric basis

The non-diagonal terms of the covariance matrix Eq. (30) in the symmetric basis are presented in Fig. 18. The terms in antisymmetric basis are omitted since they are equal to the terms in symmetric basis under a rotation of $\pi/2$ in one of the field modes [33]. The twin beams present correlation between the amplitude quadratures, $Cp_{s1}p_{s2}$ and anti-correlation between the phase quadratures, $Cq_{s1}q_{s2}$, for all values of σ in both cases, as can be seen in Fig. 18a for a $\chi^{(2)}$ gain medium and Fig. 18b for a $\chi^{(3)}$ gain medium. Both curves present a peak in the amplitude correlations ($Cp_{s0}p_{s1}$ and $Cp_{s1}p_{s2}$) associated to the peak in the amplitude noise observed in Fig. 7. The general behavior is pretty similar for the TROPO case, as showed in Fig. 20. The greatest difference among the distinct configurations is for the $\chi^{(3)}$ DROPO, where we can observe a flip on the pump-signal correlations for amplitude ($Cp_{s0}p_{s1}$) and phase quadratures ($Cq_{s0}q_{s1}$) at $\sigma \approx 3.6$, associated with the apparent disentanglement between pump and signal observed in Fig. 12.

The cross-correlations terms between symmetric and antisymmetric field modes are showed in Fig. 19 for the DROPO and Fig. 21 for the TROPO. The relevant term is $Cp_{s0}a_{s1} = -Cp_{s1}q_{a0}$ in most of the situations. Remembering that the phases of the antisymmetric basis are rotated [33], it is this the leading term associated to the apparent loss of entanglement in the tripartite case, that is recovered once the full covariance matrix is taken into account. A curious feature appears only in the $\chi^{(3)}$ case: at $\sigma = 2$ (for DROPO) or $\sigma = 4$ (for TROPO) the correlation goes to zero. That leads to a perfect decoupling of the symmetric and antisymmetric modes, as observed by the unitary value of the symplectic eigenvalue of the partially transposed matrix observed in Figs. 14 and 15.

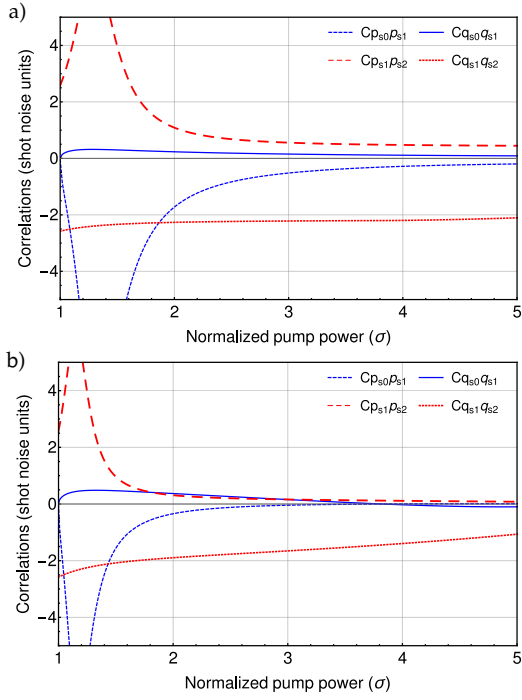


FIG. 18: DROPO: Non-diagonal elements of \mathbf{V}_s as a function of σ for $R_1 = 85\%$ and $\Omega = 0.5BW$. Considering in a) a $\chi^{(2)}$ gain medium and in b) a $\chi^{(3)}$ gain medium.

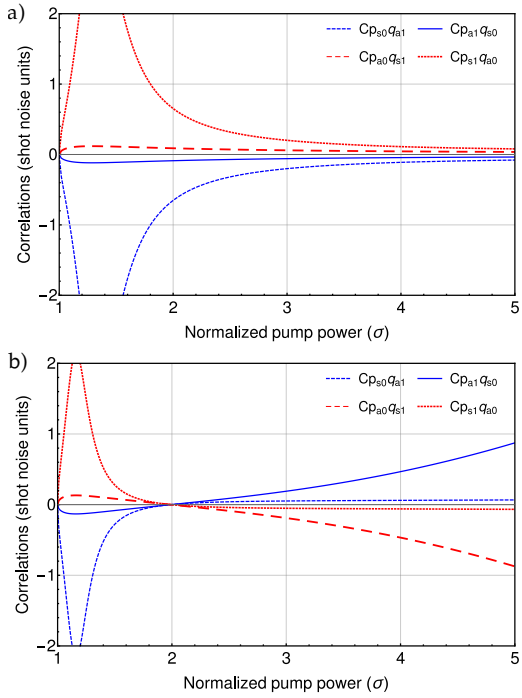


FIG. 19: DROPO: Correlations between the symmetric and antisymmetric basis as a function of σ for $R_1 = 85\%$ and $\Omega = 0.5BW$. Considering in a) a $\chi^{(2)}$ gain medium and in b) a $\chi^{(3)}$ gain medium.

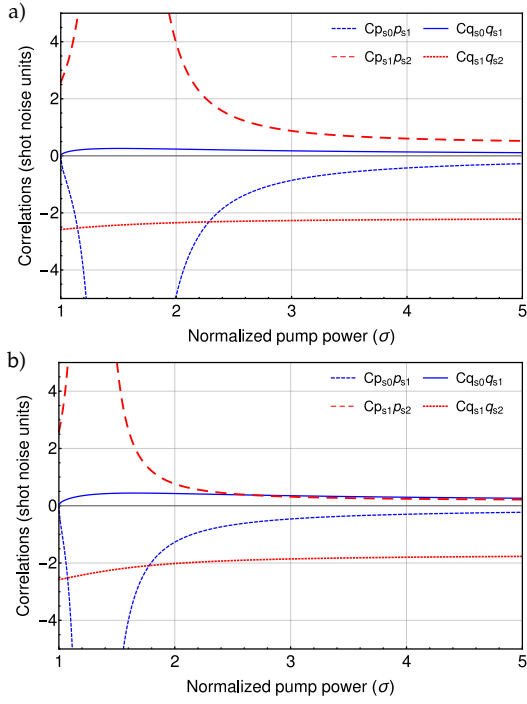


FIG. 20: TROPO: Non-diagonal elements of \mathbf{V}_s as a function of σ for $R_1 = 85\%$ and $\Omega = 0.5BW$. Considering in a) a $\chi^{(2)}$ gain medium and in b) a $\chi^{(3)}$ gain medium.

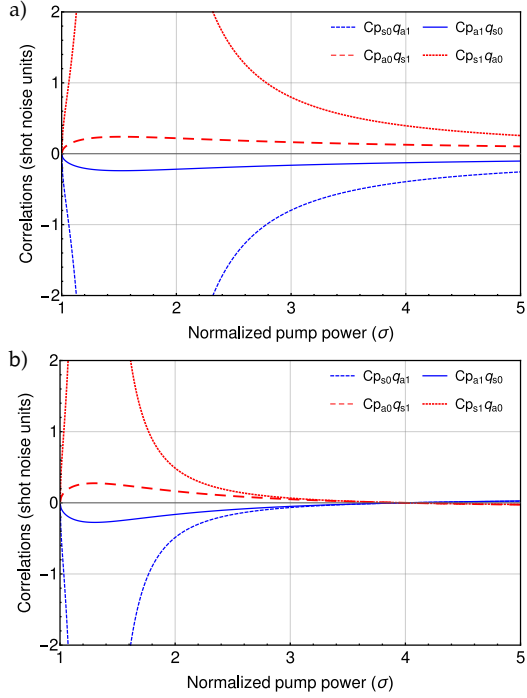


FIG. 21: TROPO: Correlations between the symmetric and antisymmetric basis as a function of σ for $R_1 = 85\%$ and $\Omega = 0.5BW$. Considering in a) a $\chi^{(2)}$ gain medium and in b) a $\chi^{(3)}$ gain medium.